4984 *Chem. Mater.* **2009,** *21,* 4984–4992
DOI:10.1021/cm902126w

CHEMISTRY OF
MATERIALS
Article

# Morphogenesis of Highly Uniform $CoCO_3$ Submicrometer Crystals and Their Conversion to Mesoporous $Co_3O_4$ for Gas-Sensing Applications

Cheng Chao Li,[†,‡] Xiao Ming Yin,[‡] Tai Hong Wang,[‡] and Hua Chun Zeng*[,†]

[†]*Department of Chemical and Biomolecular Engineering, KAUST-NUS GCR Program, and Minerals, Metals, and Materials Technology Center, Faculty of Engineering, National University of Singapore, 10 Kent Ridge Crescent, Singapore 119260, and* [‡]*Key Laboratory for Micro-Nano Optoelectronic Devices of Ministry of Education and State Key Laboratory of Chemo/Biosensing and Chemometrics, Hunan University, Changsha, 410082, P.R. China*

*Received July 14, 2009. Revised Manuscript Received September 2, 2009*

Transition metal nitrates, carbonates, hydroxides, hydroxyoxides, and so forth are often used as solid precursors to synthesize their respective nanostructured metal-oxides after chemical/thermal conversion. However, synthesis of submicrometer uniform crystalline particles of this class of compound intermediates remains as a challenging but less studied area in nanomaterials research. In this work, we report a polyol process for controlled growth of cobalt carbonate ($CoCO_3$). A preparative investigation on morphogenesis of $CoCO_3$ crystals has been carried out, and three types of highly uniform $CoCO_3$ products (i.e., peanut-like, capsule-like, and rhombus crystals) in the submicrometer region have been synthesized at 200 °C under batch conditions. Uniform particles of tricobalt tetroxide ($Co_3O_4$) have also been obtained at 300 °C from the $CoCO_3$ submicrometer crystals after thermal transformation in laboratory air. The $Co_3O_4$ powder products possess mesoporosity and essentially preserve the pristine morphologies of their respective solid precursors. Due to high crystal uniformity and specific surface areas in the range of 140−149 $m^2/g$, the mesoporous $Co_3O_4$ exhibits enhanced performances for ethanol and carbon monoxide sensing.

## Introduction

Over the past two decades, synthesis of nanoscale materials has received considerable attention in the materials research community, because electrical, optical, magnetic, and catalytic properties of the matters in this spatial scale are uniquely different from those of their corresponding bulk counterparts.[1−14] Among the numerous inorganic nanomaterials synthesized, a significant research endeavor has been devoted to prepare discrete freestanding nanoparticles, nanostructures, or their complex assemblies. For instance, many preparative methods have been developed to synthesize nanomaterials with different morphologies and architectures, such as nanoparticles, nanocubes, nanoframes, nanowires, nanobelts, nanorods, nanoflowers, nanoarrays, complex and hierarchical assemblages, and so on,[4−11] targeted directly at final functional materials and their improved properties. The morphological control, including spatial size, product shape, surface structure, and crystal orientation, of nanomaterials is of fundamental importance apart from their chemical compositions.[12−14]

Compared to the morphogenesis of discrete freestanding nanoparticles and nanostructures, morphological control of solid intermediate compounds receives much less attention. This is because in part the characterization of solid intermediates is not commonly considered to be important and in part morphologies of final products are normally different from their solid precursors due to crystallite grain boundary growth and/or agglomeration after conversion.[15−19] For example, inorganic salts such as metal nitrates and carbonates have long been used as solid precursors to prepare functional metal oxides and advanced ceramic materials through cycles of thermal annealing to deplete existing porosity and obtain high density products.[20] In the

---

*Corresponding author. Tel.: (65) 6516-2896. Fax: (65) 6779-1936. E-mail: chezhc@nus.edu.sg.

(1) Sun, S. H.; Jaouen, F.; Dodelet, J. P. *Adv. Mater.* **2008**, *20*, 3900.
(2) Kuang, Q.; Lao, C. S.; Wang, Z. L.; Xie, Z. X.; Zheng, L. S. *J. Am. Chem. Soc.* **2007**, *129*, 6070.
(3) Li, H. X.; Bian, Z. F.; Zhu, J.; Zhang, D. Q.; Li, G. S.; Huo, Y. N.; Li, H.; Lu, Y. F. *J. Am. Chem. Soc.* **2007**, *129*, 8406.
(4) Liu, B.; Zeng, H. C. *J. Am. Chem. Soc.* **2003**, *125*, 4430.
(5) Wang, X.; Li, Y. D. *J. Am. Chem. Soc.* **2002**, *124*, 2880.
(6) Lee, C. H.; Kim, M.; Kim, T.; Kim, A.; Paek, J.; Lee, J. W.; Choi, S. Y.; Kim, K.; Park, J. B.; Lee, K. *J. Am. Chem. Soc.* **2006**, *128*, 9326.
(7) Liu, H.; Hu, C. G.; Wang, Z. L. *Nano Lett.* **2006**, *6*, 1535.
(8) Oxtermann, R.; Li, D.; Yin, Y. D.; McCann, J. T.; Xia, Y. N. *Nano Lett.* **2006**, *6*, 1297.
(9) Kolmakov, A.; Klenov, D. D.; Liach, Y.; Stemmer, S.; Moskovits, M. *Nano Lett.* **2005**, *5*, 667.
(10) Joshi, R. K.; Kruis, F. E. *Appl. Phys. Lett.* **2006**, *89*, 153116.
(11) Ma, J. F.; Liang, Z.; Qiao, X. Q.; Deng, Q. L.; Tao, D. Y.; Zhang, L. H.; Zhang, Y. K. *Anal. Chem.* **2008**, *80*, 2949.
(12) Wu, B. H.; Guo, C. Y.; Zheng, N. F.; Xie, Z. X.; Stucky, G. D. *J. Am. Chem. Soc.* **2008**, *130*, 17563.
(13) Han, X. G.; Kuang, Q.; Jin, M. S.; Xie, Z. X.; Zheng, L. S. *J. Am. Chem. Soc.* **2009**, *131*, 3152.
(14) Yang, H. G.; Zeng, H. C. *Angew. Chem., Int. Ed.* **2004**, *43*, 5930.
(15) Xu, Z. P.; Zeng, H. C. *J. Mater. Chem.* **1998**, *8*, 2499.
(16) Zeng, H. C.; Lim, Y. Y. *J. Mater. Res.* **2000**, *15*, 1250.
(17) Xu, Z. P.; Zeng, H. C. *J. Phys. Chem. B* **2000**, *104*, 10206.
(18) Xu, Z. P.; Zeng, H. C. *Chem. Mater.* **2000**, *12*, 3459.
(19) Xu, R.; Zeng, H. C. *J. Phys. Chem. B* **2003**, *107*, 12643.
(20) Kingery, W. D.; Bowen, H. K.; Uhlmann, D. R. *Introduction to Ceramics*, 2nd ed.; John Wiley: New York, 1976.

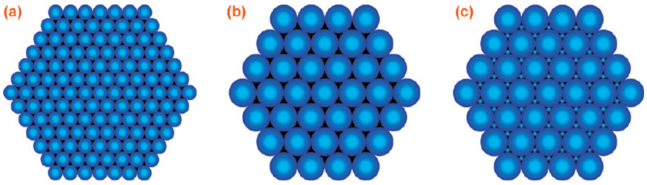

**Figure 1.** Schematic illustrations of spherical metal oxides prepared from solid precursors: (a) with small uniform particle size, (b) with large uniform particle size, and (c) with nonunifrom particle sizes. Only one layer is shown in these hexagonal close packed arrangements.

preparation of porous materials, nevertheless, it would be highly desirable to make precursor solids into uniform particles if final products can reserve their pristine crystal morphologies. In Figure 1a,b, we use hexagonal close packing of perfect spherical particles (other nonspherical particles such as ellipsoidal particles can be considered as some forms of deviation from these "perfect particles"[21]) as an example to address this point. As illustrated, perfect spheres can provide the least dense packing scheme, giving away approximately 26% of the total volume as free void space, on the basis of a simple geometric calculation.[22] Interestingly, the existence of this free void space is independent of the size of spherical particles as long as they are uniform and closely packed (i.e., Figure 1a,b).[22] On the other hand, in Figure 1c, nonuniform spheres with varying particle sizes might offer lower accessibility to reacting chemicals because the voids could be filled up with smaller particles, and interparticle space provided by them is thus lesser. Possibly, furthermore, there is a lower rate of material utilization if the particles are large (Figure 1b vs a) due to a smaller surface-area-to-bulk ratio for larger ones. Other more complex packings of particles with varying sizes can be found in the literature.[22] Apart from the free void space for reacting chemicals, small-sized monodisperse particles will allow a better utilization of materials, as larger specific surface areas can be attained if the size of particles is reduced. Therefore, use of small uniform particles is believed to be beneficial in terms of mass transport of reactants/products and cost of materials when chemical reactions are involved.

In this work, we report an investigation on the morphogenesis of cobalt carbonate ($CoCO_3$) submicrometer crystals and related preparation of highly uniform polycrystalline oxide particles of tricobalt tetroxide ($Co_3O_4$) for gas sensing applications. The targeted spinel is an important *p*-type oxide semiconductor and has aroused extensive research interest in recent years due to its potential applications as gas sensors, catalysts, electrochromic devices, and magnetic materials.[15−19,23−30] Many novel synthetic methods have been in place to make nanostructured $Co_3O_4$ with different morphologies.[31−47] Among them, a two-step approach is often adopted: (i) solid precursors containing cobalt are first synthesized, and (ii) they are then thermally converted to $Co_3O_4$. In particular, cobalt hydroxide, cobalt−nitrate−hydroxide, cobalt−nitrate−carbonate−hydroxide, and cobalt hydroxyoxide have been synthesized and demonstrated to be effective solid precursors to make $Co_3O_4$.[37−46] However, the reports on synthesis of $CoCO_3$ and using it to generate $Co_3O_4$ are rare.[47] To the best of our knowledge, synthesis of highly uniform $CoCO_3$ with particle size in the submicrometer range has not been succeeded. Herein, we developed a polyol process for controlled growth of $CoCO_3$ crystals. More specifically, morphogenesis of $CoCO_3$ has been achieved through investigating synthetic parameters, and three types of highly uniform crystals in the submicrometer region have been prepared at 200 °C under batch conditions. The as-grown $CoCO_3$ can then be converted to phase-pure mesoporous $Co_3O_4$ at a relatively low temperature of 300 °C while maintaining their pristine shapes essentially unchanged. As a result of high crystal uniformity and specific surface areas (in the range of 140−149 $m^2/g$), the derived $Co_3O_4$ shows excellent performances for ethanol and carbon monoxide sensing.

## Experimental Section

All chemicals were of analytical grade and used as received without further purification. In a typical synthesis, 0.25 g of cobalt acetate tetrahydrate [$Co(CH_3COO)_2 \cdot 4H_2O$; Nacalai

---

(21) (a) Buchalter, B. J.; Bradley, R. M. *Phys. Rev. A* **1992**, *46*, 3046. (b) Coelho, D.; Thovert, J.-F.; Adler, P. M. *Phys. Rev. E* **1997**, *55*, 1959.

(22) (a) de Larrard, F. Concrete Mixture Proportioning: A Scientific Approach. *Modern Concrete Technology Series*, No. 9; E & FN SPON: London, U.K., 1999. (b) A simple mathematical derivation is as follows. Face centered cubic unit cell: 4 spheres per unit cell (R is radius of sphere). Volumn of unit cell (face centered cubic): $V_2 = [2(\sqrt{2})R]^3 = 16(\sqrt{2})R^3$. Volumn of spheres inside unit cell: $V_1 = 4(4/3)\pi R^3 = (16/3)\pi R^3$. Volumn of void space: $V_2 - V_1 = 16(\sqrt{2})R^3 - (16/3)\pi R^3 = [16(\sqrt{2}) - (16/3)\pi]R^3$

$$\frac{V_2 - V_1}{V_2} = \frac{\left(16\sqrt{2} - \frac{16}{3}\pi\right)R^3}{16\sqrt{2}R^3} = \frac{\sqrt{2} - \frac{\pi}{3}}{\sqrt{2}} \approx 26\%$$

$$\frac{V_1}{V_2} = \frac{\frac{16}{3}\pi R^3}{16\sqrt{2}R^3} = \frac{\pi}{3\sqrt{2}} \approx 74\%$$

(23) Dong, Z.; Fu, Y. Y.; Han, Q.; Xu, Y. Y.; Zhang, H. *J. Phys. Chem. C* **2007**, *111*, 18475.

(24) Binotto, G.; Larcher, D.; Prakash, A. S.; Urbina, R. H.; Hegde, M. S.; Tarascon, J. M. *Chem. Mater.* **2007**, *19*, 3032.

(25) Zhan, F. M.; Geng, B. Y.; Guo, Y. J. *Chem.—Eur. J.* **2009**, *15*, 6169.

(26) Xiong, S. L.; Yuan, C. Z.; Zhang, X. G.; Xi, B. J.; Qian, Y. T. *Chem.—Eur. J.* **2009**, *15*, 5320.

(27) Cao, D. X.; Chao, J. D.; Sun, L. M.; Wang, G. L. *J. Power Sources* **2008**, *179*, 87.

(28) Li, W. Y.; Xu, L. N.; Chen, J. *Adv. Funct. Mater.* **2005**, *15*, 851.

(29) Wollenstein, J.; Burgmair, M.; Plescher, G; Sulima, T.; Hildenbrand, J; Bottner, H.; Eisele, I. *Sens. Acuators, B* **2003**, *93*, 442.

(30) Jana, N. R.; Chen, Y. F.; Peng, X. G. *Chem. Mater.* **2004**, *16*, 3931.

(31) He, T.; Chen, D. R.; Jiao, X. L.; Xu, Y. Y.; Gu, Y. X. *Langmuir* **2004**, *20*, 8404.

(32) He, T.; Chen, D. R.; Jiao, X. L. *Chem. Mater.* **2004**, *16*, 737.

(33) Chen, C. H.; Abbs, S. F.; Morey, A.; Sithambaram, S.; Xu, L. P.; Garces, H. F.; Hines, W. A.; Suib, S. L. *Adv. Mater.* **2008**, *20*, 1205.

(34) Hu, L. H.; Peng, Q.; Li, Y. D. *J. Am. Chem. Soc.* **2008**, *130*, 16136.

(35) Li, Y. G.; Tan, B.; Wu, Y. Y. *J. Am. Chem. Soc.* **2006**, *128*, 14258.

(36) Tüysüz, H.; Comotti, M.; Schüth, F. *Chem. Commun.* **2008**, *14*, 4022.

(37) Nethravathi, C.; Sen, S.; Ravishankar, N.; Rajamathi, M.; Pietzonka, C.; Harbrecht, B. *J. Phys. Chem. B* **2005**, *109*, 11468.

(38) Ding, Y. S.; Xu, L. P.; Chen, C. H.; Shen, X. F.; Suib, S. L. *J. Phys. Chem. C* **2008**, *112*, 8177.

(39) Hosono, E.; Fujihara, S.; Honma, I.; Zhou, H. S. *J. Mater. Chem.* **2005**, *15*, 1938.

(40) Zhao, Z. G.; Geng, F. X.; Bai, J. B.; Cheng, H. M. *J. Phys. Chem. C* **2007**, *111*, 3848.

(41) Geng, B. Y.; Zhan, F. M.; Fang, C. H.; Yu, N. *J. Mater. Chem.* **2008**, *18*, 4977.

(42) Lou, X. W.; Deng, D.; Lee, J. Y.; Archer, L. A. *J. Mater. Chem.* **2008**, *18*, 4397.

(43) Xu, R.; Zeng, H. C. *J. Phys. Chem. B* **2003**, *107*, 926.

(44) Feng, J.; Zeng, H. C. *Chem. Mater.* **2003**, *15*, 2829.

(45) Feng, J.; Zeng, H. C. *J. Phys. Chem. B* **2005**, *109*, 17113.

(46) Zhang, H.; Wu, J. B.; Zhai, C. X.; Ma, X. Y.; Du, N.; Tu, J. P.; Yang, D. R. *Nanotechnology* **2008**, *19*, 035711.

(47) Cong, H. P.; Yu, S. H. *Cryst. Growth Des.* **2009**, *9*, 210.

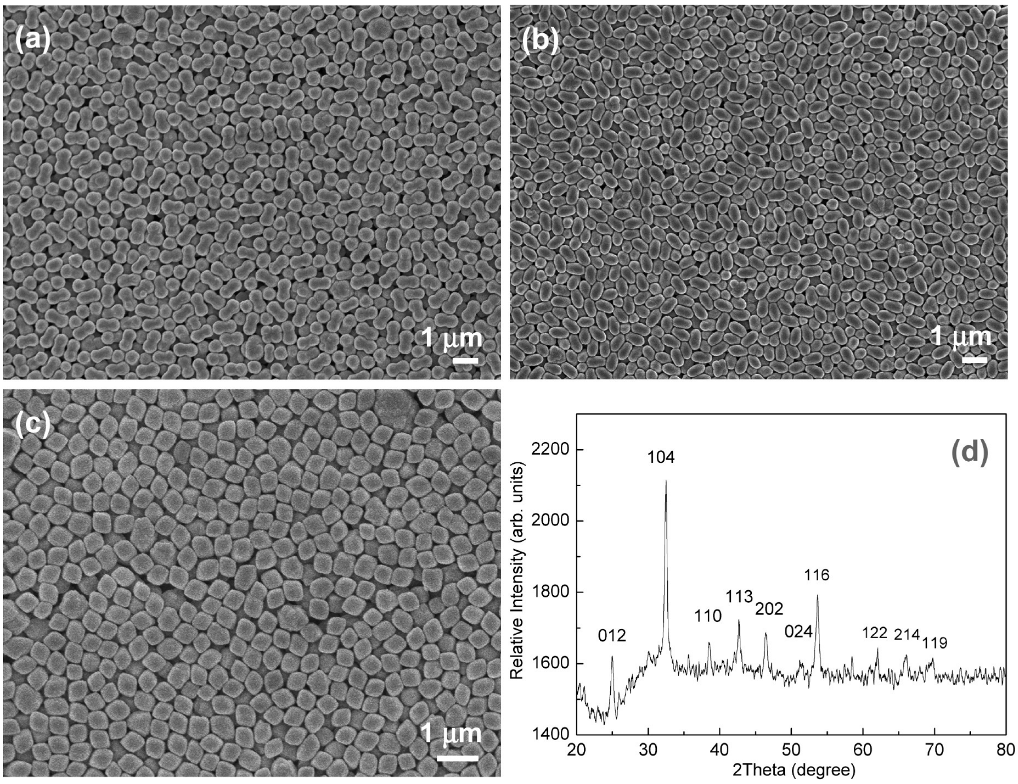

**Figure 2.** FESEM images of our three types of samples: (a) peanut-like, (b) capsule-like, and (c) rhombus $CoCO_3$ crystals. A typical XRD pattern of these $CoCO_3$ crystals is also displayed in (d).

tesque, Inc.] and 0.5 g of polyvinyl-pyrrolidone (PVP; MW = 40 000, K30, Fluka) were first dissolved in 20 mL of diethylene glycol (DEG; $C_4H_{10}O_3$; Sigma-Aldrich) at room temperature, followed by addition of a varying amount of urea (0.25−1.0 g; $CO(NH_2)_2$; Fluka) under vigorous stirring. Then the mixture was transferred to a Teflon-lined stainless steel autoclave and kept inside an electric oven at 200 °C for a certain reaction period, typically 12 to 21 h. After reactions, pink solid products of cobalt carbonate ($CoCO_3$) in the bottom of the autoclave were harvested, washed with deionized water and ethanol several times via centrifugation−redispersion cycles, and then dried in an oven at 80 °C for 12 h. In laboratory air, the thus-prepared $CoCO_3$ was converted to mesoporous tricobalt tetroxide ($Co_3O_4$) by thermal decomposition at 300 °C for 4 h with an electric furnace.

Crystallographic phases of the above prepared products were investigated by powder X-ray diffraction method (XRD) using a Shimadzu XRD-6000 diffractometer with Cu Kα radiation. Morphologies of samples were characterized by field-emission scanning electron microscopy (FESEM; JSM-6700F), selected area electron diffraction (SAED), transmission electron microscopy (TEM/SAED; JEM-2010, 200 kV), and high-resolution TEM (HRTEM/SAED; JEOL-2100F, 200 kV). Fourier transform infrared (FTIR) spectra were record for samples using the KBr powder technique (Bio-Rad FTS-135 FTIR spectrometer). Surface analysis of samples was carried out with X-ray photoelectron spectroscopy (XPS, AXIS-HSi, Kratos Analytical). A monochromated Al Kα (1486.6 eV) radiation was used as an excitation source, and the measurement was done with constant analyzer energy mode at 40 eV. All binding energies were referenced to the C 1s peak (284.6 eV) arising from surface hydrocarbons (or adventitious hydrocarbons). Thermogravimetric analysis (TGA; Shimadzu TGA-50) was also conducted to determine the composition of samples. The TGA measurements were carried out at a heating rate of 10 °C/min from 50 to 900 °C with an air flow rate of 100 mL/min. Measurement of specific surface area and analysis of porosity for the $Co_3O_4$ products were performed through measuring $N_2$ adsorption−desorption isotherms at 77 K with a Quantachrome NOVA-3000 system.

The gas sensors were fabricated as follows. The as-prepared $Co_3O_4$ products were mixed with ethanol and hand-ground in an agate mortar to form black slurries. The prepared slurries were then laid uniformly on the surfaces of ceramic tubes used to form sensors. Two Pt electrodes were fabricated on the tubes near the two ends, and a heating resistance coil was inserted through the central space of the ceramic tubes. A similar device configuration for other sensors had been sketched in the literature.[48] The prepared sensors were then annealed at 300 °C for 2 h in a muffle furnace, followed by a 24 h aging process in laboratory air, as described earlier.[48] In our sensing measurements, the gas sensors were connected in series with a standard resistor. Under an applied voltage of 5 V, the voltage across the standard resistor was measured to evaluate the electrical resistance of the sensors. The resistance changed after putting the sensors into a gas chamber, which was installed with test gases at different concentrations. Ethanol sensing tests were carried out by injecting a certain volume of liquid ethanol calculated with an assumption that all the ethanol would be gasified. Furthermore, carbon monoxide sensing tests were also done by introducing a standard CO into the gas chamber. The sensing properties were investigated under a range of concentrations of target gases at 300 °C and ambient relative humidity of 57%.

## Results and Discussion

Morphologies of the as-prepared $CoCO_3$ submicrometer crystals were examined with FESEM. Figure 2

---

(48) Liang, Y. X.; Chen, Y. J.; Wang, T. H. *Appl. Phys. Lett.* **2004**, *85*, 666.

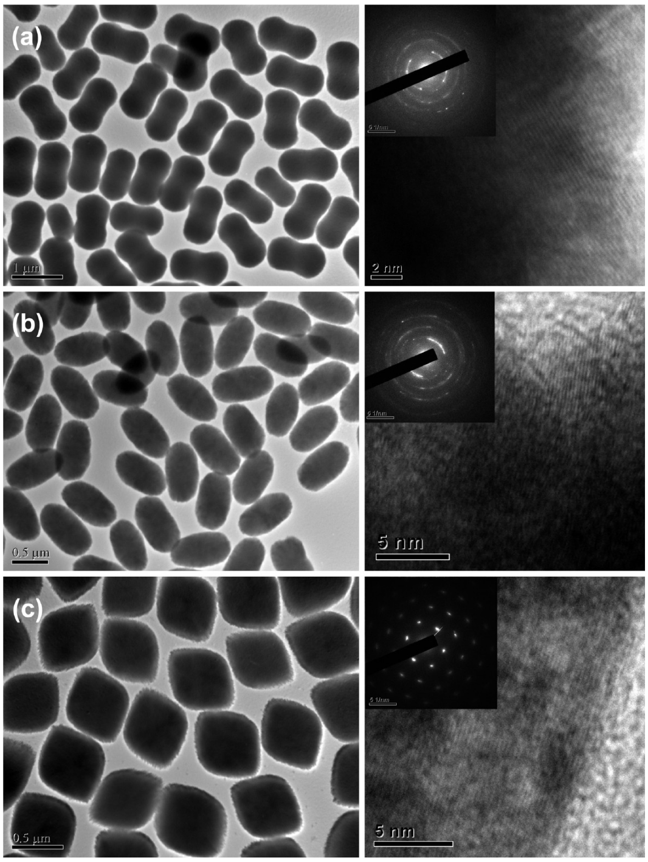

**Figure 3.** TEM images, HRTEM images and SAED patterns of our three types of samples: (a) peanut-like, (b) capsule-like, and (c) rhombus $CoCO_3$ crystals.

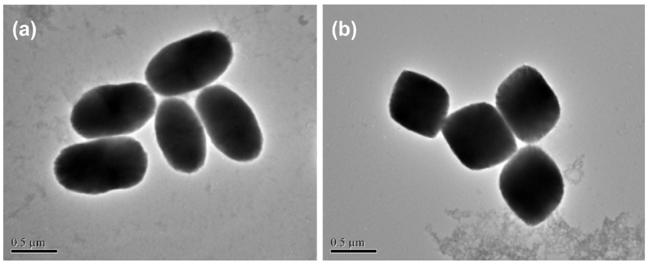

**Figure 4.** TEM images of (a) capsule-like and (b) rhombus $CoCO_3$ crystals synthesized after 6 h of reaction, together with some amorphous deposits in the image backgrounds.

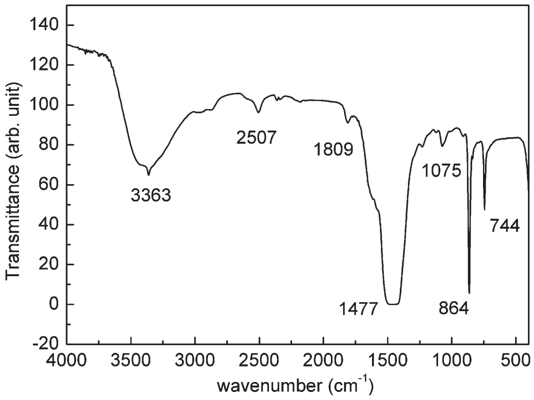

**Figure 5.** Typical FTIR spectrum of the $CoCO_3$ crystals prepared in this work.

displays some typical FESEM images of $CoCO_3$ products prepared with the present approach as a function of urea concentration (see Experimental Section). As reported, the $CoCO_3$ crystals are highly uniform with a diameter range at around 500 nm. Through changing the concentration of urea (Figure 2a−c), fine morphogenesis of $CoCO_3$ crystals has been achieved. In particular, peanut-like, capsule-like, and rhombus products can be synthesized with 0.25, 0.50, and 0.75−1.0 g of urea, respectively, while keeping other process parameters unaltered. In general, these crystal particles can be viewed as approximated forms of ellipsoid, and their packing is amorphous due to short aspect ratios, although some localized ordering can still be observed (Figure 2). The crystal structures of the samples were further characterized by TEM and HRTEM/SAED methods. Figure 3 shows the TEM/HRTEM images and SAED patterns for the three types of samples reported in Figure 2. With the increase in urea in synthesis, crystallinity of the samples increases. In fact, single-crystalline $CoCO_3$ (rhombus submicrometer crystals, see Figure 3c and the related SAED pattern) could be obtained when the urea content was increased to a range of 0.75−1.0 g (i.e., mole ratio uera/$Co^{2+}$ = 12.5−16.7). When the urea content was lower, the resultant peanut-like (i.e., mole ratio uera/$Co^{2+}$ = 4.2) and capsule-like $CoCO_3$ (i.e., mole ratio uera/$Co^{2+}$ = 8.3) became more polycrystalline, as shown in the ring-like structures of their respective SAED patterns, although the lattice fringes in the HRTEM images were all measured at a value of $d_{104} = 2.7 \pm 0.1$ Å. Nonetheless, the long-range order of crystal lattices in the two samples is still present, since coherent regions of lattice fringes in the images are fairly large (e.g., across entire HRTEM images in Figure 3a,b) and brighter segments in the diffraction rings can be observed, which implies a substantial amount of crystallites in these two samples are crystallographically oriented.[49−53] The crystal phase of these $CoCO_3$ samples was also identified by powder XRD technique; a representative diffraction pattern is shown in Figure 2d. As expected, the peaks can be indexed to the rhombohedral phase of $CoCO_3$ (space group $R\bar{3}c$, JCPDS PDF file no. 11-0692; $a_0$ = 4.659 Å and $c_0$ = 14.96 Å), and the absence of other diffraction peaks affirms the generation of phase-pure $CoCO_3$ submicrometer crystals.

As revealed by the above characterization, the $CoCO_3$ submicrometer crystals were formed by aggregative attachment of even smaller crystallites during our syntheses. All three $CoCO_3$ samples with high product uniformity could be prepared respectively with reaction times over a range of 12 to 21 h. The formation pathway of these $CoCO_3$ submicrometer crystals is explained by a mechanism of precipitation−dissolution−renucleation−growth−aggregation. In an initial stage, primary precipitates

---

(49) Penn, R. L.; Banfield, J. F. *Science* **1998**, *281*, 969.

(50) Pacholski, C.; Kornowski, A.; Weller, H. *Angew. Chem., Int. Ed.* **2002**, *41*, 1188.

(51) Liu, B.; Zeng, H. C. *J. Am. Chem. Soc.* **2003**, *125*, 4430.

(52) Penn, R. L. J. Phys. Chem. B **2004**, *108*, 12707 and the references therein.

(53) Zeng, H. C. *Int. J. Nanotechnol.* **2007**, *4*, 329.

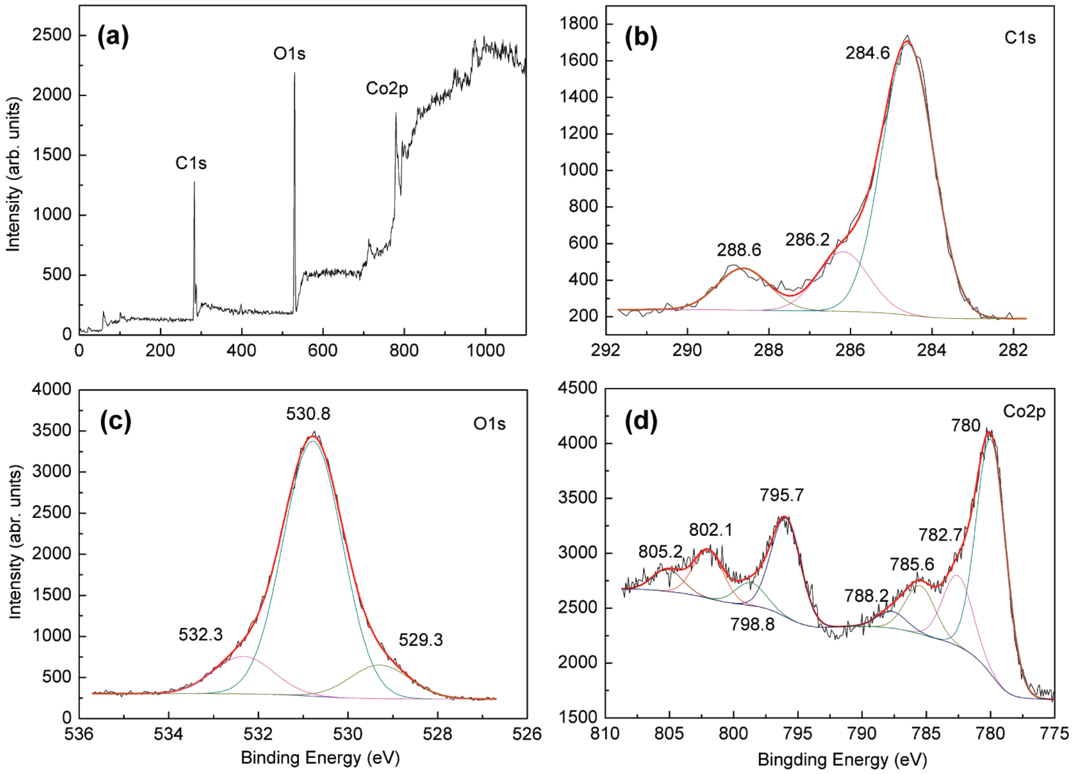

**Figure 6.** Representative XPS spectra of the $CoCO_3$ crystals: (a) wide scan, (b) C 1s, (c) O 1s, and (d) Co 2p.

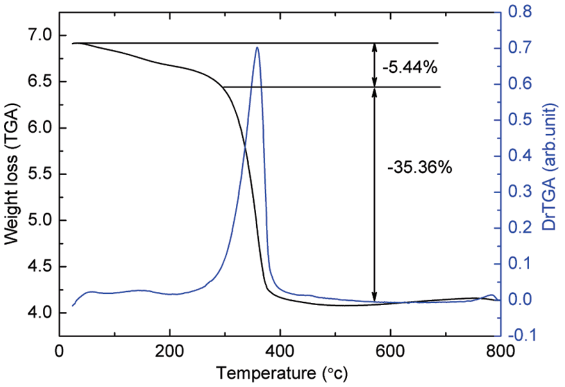

**Figure 7.** TGA and DrTGA curves of the $CoCO_3$ crystals.

were formed instantaneously when supersaturation in the solution phase was reached. The process was followed by dissolution of unstable precipitates which was then turned into renucleation and growth of crystallites.[47,54−56] The resultant crystallites were aggregated and/or attached into final crystals, as commonly described in mineralization processes.[52,53] In this agreement, the proposed pathway is supported by our time-dependent experiments. As shown in Figure 4, when the reaction time was reduced to 6−9 h, the peanut-like product could not be prepared, whereas the capsule-like or rhombus products were already present. Furthermore, primary precipitates (amorphous) accompanied with the desired crystal products (Figure 4) can be detected, which could be converted to the $CoCO_3$ phase completely when the reaction time was prolonged. The carbonate anions in the synthesis were supplied from urea. When heated at about 90 °C, urea is burst thermally into $CO_2$ and $OH^-$ (eq 1). Because the formation of carbonate largely depends on the dissolution of $CO_2$ gas (eq 2) under closed reaction conditions, $CoCO_3$ becomes more difficult to form when the amount of urea supply in the synthesis is on the lower side (eq 3). As compared in Figure 4, the formation of peanut-like $CoCO_3$ was indeed the most difficult, although the urea used in the synthesis (mole ratio uera/$Co^{2+}$ = 4.2) still exceeded its stoichiometric ratio.

$$CO(NH_2)_2 + 3H_2O \rightarrow 2NH_4^+ + CO_2 + 2OH^- \qquad (1)$$

$$2NH_4^+ + CO_2 + 2OH^- \rightarrow 2NH_4^+ + CO_3^{2-} + H_2O \qquad (2)$$

$$Co^{2+} + CO_3^{2-} \rightarrow CoCO_3 \qquad (3)$$

To reveal the chemical composition and bonding situation of pink-colored $CoCO_3$ crystals, the FTIR investigation has been carried out. Figure 5 presents a typical FTIR spectrum of the as-prepared $CoCO_3$ samples. The band at around 3442 $cm^{-1}$ is assigned to the stretching vibration of the O−H group of surface adsorbed molecular water and hydrogen-bound O−H, and the sharp

---

(54) Gao, A. M.; Hu, J. S.; Liang, H. P.; Song, W. G.; Wan, L. J.; He, X. L.; Gao, X. G.; Xia, S. H. *J. Phys. Chem. B* **2006**, *110*, 15858.
(55) Hou, B; Li, Z. J.; Xu, Y.; Wu, D.; Sun, Y. H. *J. Electroceram.* **2006**, *16*, 127.
(56) Yu, S. H.; Cölfen, H.; Antonietti, M. *J. Phys. Chem. B* **2003**, *107*, 7396.

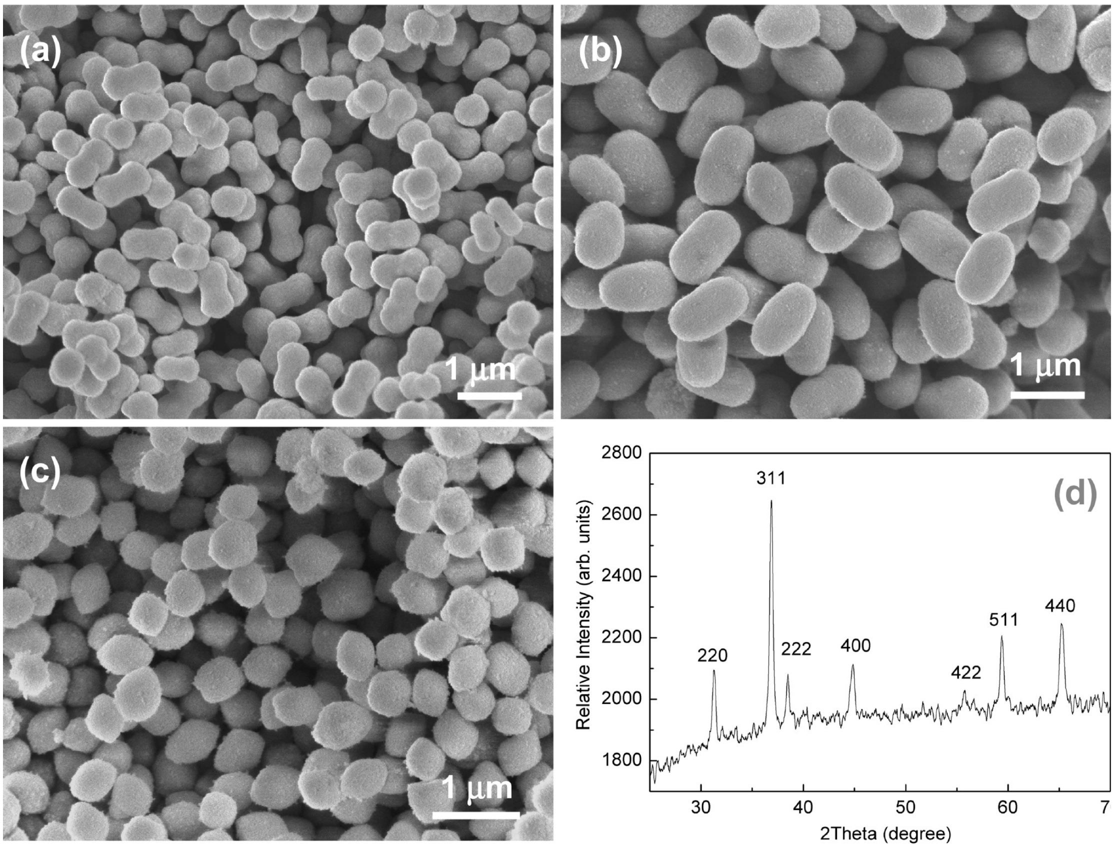

**Figure 8.** FESEM images of our $Co_3O_4$ spinel oxide samples prepared from three solid precursors: (a) peanut-like, (b) capsule-like, and (c) rhombus $CoCO_3$ crystals after a heat-treatment at 300 °C. A typical XRD pattern of these $Co_3O_4$ crystals is also displayed in (d).

peak centered at around 3363 $cm^{-1}$ is attributed to the O$-$H groups interacting with carbonate anions of the $CoCO_3$.[15,47] The presence of $CO_3^{2-}$ in the cobalt carbonate sample is evidenced by its fingerprint peaks of $D_{3h}$ symmetry at 1477, 1075, 864, and 744 $cm^{-1}$, which are assigned to vibrational modes of $\nu_3(E')$, $\nu_1(A'_1)$, $\nu_2(A''_1)$ and $\nu_4(E'')$, respectively, according to normal modes of vibration of planar $XO_3$ molecules/ions (X = C in the present case);[57] the peak located at 2507 $cm^{-1}$ is also commonly associated to a vibrational mode of carbonate anion.[57] The weak peak at 1809 $cm^{-1}$ is attributed to an overtone or combination band composed of contributions from the combination of some vibrational modes of the carbonate groups and divalent metal ions.[57] To have further information on surface composition of the samples, XPS analysis has been performed in this work. Figure 6a shows a wide scan spectrum of the as-prepared sample. The peaks located at 284.6, 531.8, and 780.8 eV are assigned to the characteristic peaks of C 1s, O 1s, and Co 2p, respectively.[58] As expected, the above sharp peaks confirm the abundant existence of carbon, oxygen, and cobalt elements on the sample surfaces of $CoCO_3$. The peaks at 288.6 eV in the C 1s spectrum is assigned to the carbon element in association with oxygen in the carbonate ions.[58−60] The peaks at 284.6 and 286.2 eV can be attributed generally to surface-adsorbed hydrocarbons and their oxidative forms (e.g., C$-$OH).[58−60] The predominant O 1s peak at 530.8 eV belongs to the lattice oxygen of $CoCO_3$, and the other two peaks at 529.3 and 532.3 eV can be assigned to oxygen species in surface-adsorbed DEG and $H_2O$ molecules, respectively.[58−60] The core level peaks of Co 2p at 780.0 and 795.7 eV correspond to Co $2p_{3/2}$ and Co $2p_{1/2}$ of $CoCO_3$ and its surface oxidized product $Co_3O_4$. The Co 2p peaks at 782.7 (Co $2p_{3/2}$) and 798.8 (Co $2p_{1/2}$) eV can be assigned to the CoO surface phase which is in equilibrium with $Co_3O_4$.[58−60] The remaining smaller peaks at higher binding energies (785.6, 788.2, 802.1, and 805.2 eV) are satellite shake-ups of the assigned components, respectively. The thermal behavior of the $CoCO_3$ samples has also been investigated by TGA technique, as presented in Figure 7. The total weight loss of the sample in the heat-treatment was determined to be 40.8%. The first weight loss of about 5.44% was mainly due to the elimination of absorbed/trapped water molecules or surfactants in the sample. When the temperature is above 300 °C, the rate of weight loss became fast, which could be attributed to the decomposition of $CoCO_3$ into $Co_3O_4$ and $CO_2$ in

---

(57) (a) Ehlsissen, K. T.; Delahaya-Vidal, A.; Genin, P.; Figlarz, M.; Willmann, P. *J. Mater. Chem.* **1993**, *3*, 883. (b) Tatzber, M.; Stemmer, M.; Spiegel, H.; Katzlberger, C.; Haberhauer, G.; Gerzabek, M. H. *Envoron. Chem. Lett.* **2007**, *5*, 9.

(58) Wagner, C. D.; Riggs, W. M.; Davis, L. E.; Moulder, J. E.; Muilenber, G. E. *Handbook of X-ray Photoelectron Spectroscopy*; Perkin-Elmer: Eden Prairie, MN, U.S.A., 1979.

(59) Xu, R.; Zeng, H. C. *Langmuir* **2004**, *20*, 9780.

(60) Chen, H. M.; Liu, R.-S.; Li, H. L.; Zeng, H. C. *Angew. Chem., Int. Ed.* **2006**, 45 2713.

the presence of oxygen from the flowing air stream of TGA:

$$6CoCO_3 + O_2 \rightarrow 2Co_3O_4 + 6CO_2 \qquad (4)$$

The actual weight loss of $CoCO_3$ to $Co_3O_4$ in this thermal process was about 35.36%, which is slightly higher than the theoretically calculated value (32.51%), noting that some deep-trapped organic matter (PVP and/or DEG) was also burnt over this temperature range.

After being calcined at 300 °C for 4 h, the as-synthesized $CoCO_3$ crystals were converted completely into phase-pure cobalt oxide $Co_3O_4$. Figure 8a–c presents FESEM images of the three different types of $Co_3O_4$ products from this oxidative heat-treatment. The pristine morphologies of the $CoCO_3$ crystals were well preserved in their oxide products, and no appreciable shape and size changes were observed. However, their surfaces seem to become rougher, suggesting the generation of porous $Co_3O_4$ through the calcination. The crystallographic phase of this spinel oxide was confirmed by the XRD method, as displayed in Figure 8d. All the diffraction peaks can be assigned to the cubic phase of $Co_3O_4$ (space group $Fd\bar{3}m$; lattice constant $a_0$ = 8.0837 Å; JCPDS PDF file no. 42-1467).[43–45] The textural properties of the $Co_3O_4$ samples were further investigated by measuring adsorption/desorption isotherms of nitrogen at 77 K, as shown in Figure 9. The hysteresis features of peanut-like $Co_3O_4$ sample at the relative pressures of 0.6–0.9 should be classified as type H3 loop, which does not show any limiting adsorption at the higher side of this relative pressure range (Figure 9a), suggesting the presence of aggregates of plate-like particles which give rise to slit-shaped pores.[61] The following abrupt increase in the curves at high relative pressure, above 0.9, can be ascribed to the multilayer adsorption of nitrogen in the macropores formed among the resultant $Co_3O_4$ nanocrystallites. From the pore distribution curves, it can also be found that the peanut-like $Co_3O_4$ nanostructures have a bimodal pore distribution using the Barrett–Joyner–Halenda (BJH) method, that is, smaller pores in region of 20–30 nm, and the larger pores ranging from 40 to 120 nm. The specific surface area using the Brunauer–Emmett–Teller (BET) method for this sample is 148.9 $m^2$/g. Similarly, the isotherms of capsule-like and rhombus $Co_3O_4$ products also showed mesoporous structural characteristics, as shown in Figure 9b,c. Specific surface areas for the latter two samples are 140.4 and 143.3 $m^2$/g, respectively. Different from the peanut-like $Co_3O_4$ sample, however, capsule-like and rhombus $Co_3O_4$ nanostructures only show a monomodal pore distribution, which ranges from 20 to 50 nm and from 18 to 45 nm, respectively, for the two samples. The hysteresis loops of the capsule-like and rhombus $Co_3O_4$ products both also belong to type IV isotherms, but they have H1 type hysteresis loops instead of H3 type, which are known from the formation of agglomerates or compacts of approximately uniform crystallites in fairly regular arrays and hence the narrow distributions of the resultant pore size.[61]

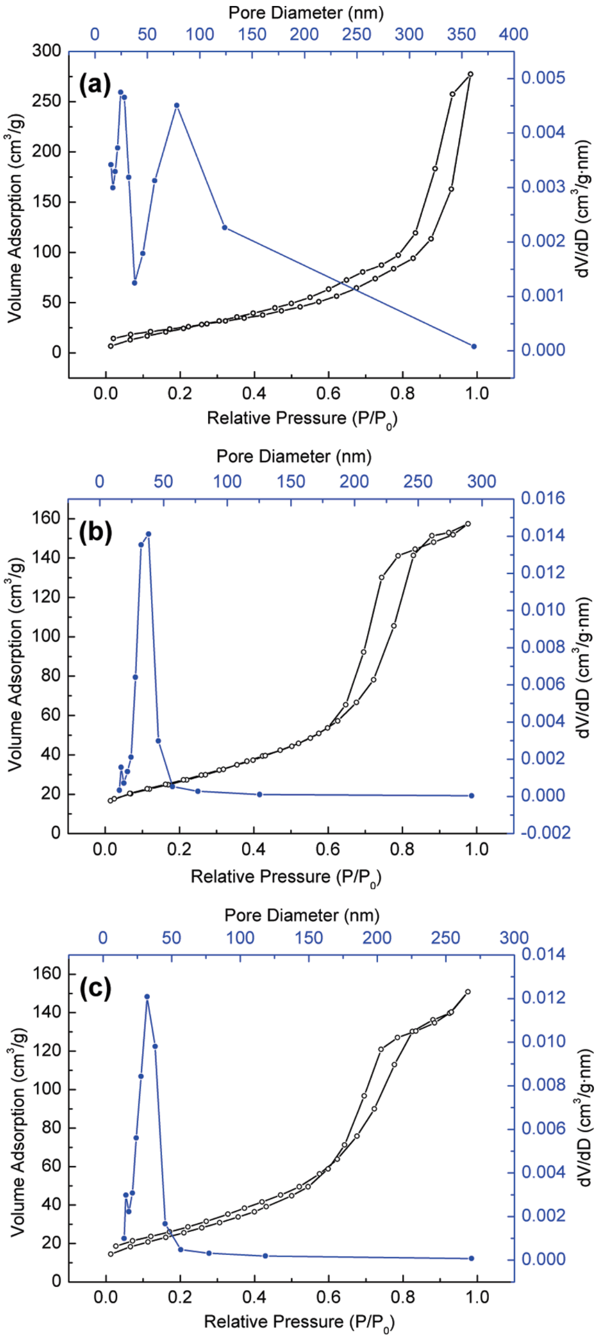

**Figure 9.** Nitrogen physisorption isotherms and pore size distribution curves of (a) peanut-like, (b) capsule-like, and (c) rhombus mesoporous $Co_3O_4$ samples (also see Figure 8).

As a result of the large surface areas and mesoporosity revealed in the $Co_3O_4$ samples, these nanostructured oxides might be advantageous for gas sensing applications. Therefore, conductometric properties of mesoporous $Co_3O_4$ samples to ethanol and carbon monoxide have also been investigated in this work. Figure 10i presents our ethanol sensing results from the porous $Co_3O_4$ at a working temperature of 300 °C. The response curves show the *on* and *off* characteristics of the three sensors when they were inserted into and taken out of the gas chamber. With increasing

---

(61) Sing, K. S. W.; Everett, D. H.; Haul, R. A. W.; Moscou, L.; Pierotti, R. A.; Rouquerol, J.; Siemieniewska, T. *Pure Appl. Chem.* **1985**, *57*, 603.

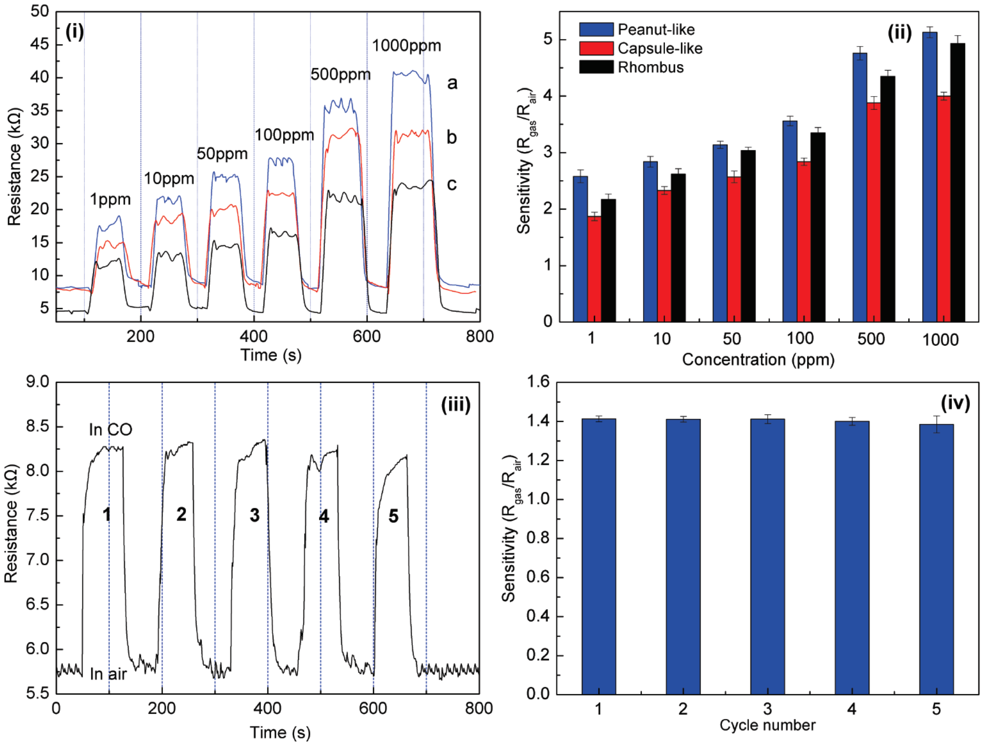

**Figure 10.** Gas-sensing applications: (i) ethanol sensing curves of the synthesized mesoporous $Co_3O_4$ (a: peanut-like, b: capsule-like, and c: rhombus) with different ethanol concentrations (1 to 1000 ppm), (ii) sensitivities calculated from (i), (iii) carbon monoxide sensing curves of peanut-like mesoporous $Co_3O_4$ with a CO concentration at 10 ppb, and (iv) sensitivities calculated from (iii).

ethanol concentrations, the resistance of sensor increased monotonically. In particular, the sensitivity (Figure 10ii) is proportional to the specific surface areas, that is, 148.9, 140.4, and 143.3 $m^2/g$, of the three samples. The peanut-like $Co_3O_4$ shows a slightly better performance than the other two $Co_3O_4$ nanostructures despite having the same detection limit. The better response in the peanut-like $Co_3O_4$ can be associated to the presence of additional macroporous structure in this sample (Figure 9a). For metal-oxide semiconductor based gas sensors, changes in electrical resistance are mainly caused by the adsorption and desorption of oxygen species and targeted analytes on the surface of sensing materials. Therefore, the larger surface area of sensing materials normally results in more active sites on the surface for chemical or physical interactions. On the other hand, bigger pore size would ease gaseous molecules to enter the pores and migrate to active sites. Compared to those realized from *n*-type semiconductor oxides such as ZnO,[62,63] $In_2O_3$,[64,65] and $SnO_2$,[66,67] our $Co_3O_4$ sensors have exhibited comparable sensitivity ($R_{gas}/R_{air}$), reversibility, and an even lower detection limit. As a comparison, the commercial breath analyzers (mainly using *n*-type oxides) only have a detection limit of 10 to 200 ppm whereas our sensors reduce this limit down to 1 ppm (Figure 10i). Generally speaking, the difference in sensitivity between *p*-type and *n*-type semiconductor oxides lies on different conductometric mechanisms. For instance, in the *n*-type semiconductor oxides, the electron conduction is dominant. When such a sensor is operated in air, oxygen molecules adsorb on the surface of sensing material and capture free electrons from the surface to form negatively charged ions ($O^-$, $O_2^-$, and $O^{2-}$), which results in the increase of resistance of gas sensor due to the depletion of carrier electrons. When the sensor is put in the chamber containing ethanol vapor, the adsorbed oxygen anions will react with ethanol molecules and release the electrons back to the conduction band of *n*-type oxides, leading to a sharp decrease of resistance. On the contrary, fewer oxygen molecules will adsorb on the surfaces of *p*-type sensing oxides because positive holes are the major charge carriers and the surface concentration of electrons is lower compared to that in the *n*-type oxides. Nonetheless, the adsorption of gaseous oxygen results in decrease of electrical resistance due to a better separation of holes from the electrons. When a *p*-type sensor is exposed to ethanol gas, electrons are released back to the conduction band and recombine with holes, which decrease the carrier concentration (holes) and thus increase the sensor resistance (Figure 10iii). To further extend the sensing applications of our $Co_3O_4$, we also investigated its carbon monoxide sensing properties (Figure 10iii,iv).[68,69] In Figure 10iii, the CO sensing

---

(62) Jing, Z. H.; Zhan, J. H. *Adv. Mater.* **2008**, *20*, 4547.
(63) Li, C. C.; Du, Z. F.; Li, L. M.; Yu, H. C.; Wan, Q.; Wang, T. H. *Appl. Phys. Lett.* **2007**, *91*, 032101.
(64) Li, C.; Zhang, D. H.; Lie, B.; Han, S.; Liu, X. L.; Zhou, C. W. *J. Phys. Chem. B* **2003**, *107*, 12451.
(65) Li, E.; Cheng, Z. X.; Xu, J. Q.; Pan, Q. Y.; Yu, W. J.; Chu, Y. L. *Cryst. Growth Des.* **2009**, *9*, 2146.
(66) Comini, E.; Faglia, G.; Sberveglieri, G.; Pan, Z. W.; Wang, Z. L. *Appl. Phys. Lett.* **2002**, *81*, 1869.
(67) Wang, Y. L.; Jiang, X. C.; Xia, Y. N. *J. Am. Chem. Soc.* **2003**, *125*, 16176.
(68) Li, N.; Tan, T. C.; Zeng, H. C. *J. Electrochem. Soc.* **1993**, *140*, 1068.
(69) Cantalini, C.; Post, M.; Buso, D.; Guglielmi, M.; Martucci, A. *Sens. Acuators, B* **2005**, *108*, 184.

performance of the peanut-like $Co_3O_4$ sample has been presented as a dynamic responsive curve. When the sensor was exposed to 10 ppb of CO, the resistance promptly increased and then reached a relatively stable value. When the sensor was switched to air atmosphere again, the resistance dropped sharply to the baseline. A total of five periods have been tested at this CO concentration, and the response and recovery time is only about 20 s. The threshold limit of CO for the human body is only about 3−5 ppm, and it becomes dangerous if a CO concentration is higher than 15 ppm. The detection limit in Figure 10iii is very low, compared to what has been reported in the literature.[29,54,68,69] Using hierarchically structured $Co_3O_4$, for example, the sensitivity of the sensors was about 1.8 when the concentration of CO was 1000 ppm.[54] Therefore, we have also demonstrated that the mesoporous $Co_3O_4$ with submicrometer particle size is a promising material for future development of CO gas sensors, apart from its good sensing ability for ethanol.

## Conclusions

In summary, we have developed a polyol based approach for preparation of highly uniform submicrometer crystals of $CoCO_3$ with the assistance of PVP in DEG. Under batch conditions, by varying the concentration of urea in synthesis, peanut-like, capsule-like, and rhombus $CoCO_3$ crystals have been synthesized respectively at 200 °C for a period of 12−21 h. On the basis of our time-dependent synthetic experiments and materials characterization, the formation of these $CoCO_3$ crystals can be attributed to a precipitation−dissolution−renucleation−growth−aggregation process. In air atmosphere, uniform metal oxide particles of $Co_3O_4$ have also been obtained from their respective $CoCO_3$ submicrometer crystals after oxidative thermal decomposition at 300 °C for 4 h. Our surface textural/morphological investigation further reveals that the thermally converted $Co_3O_4$ products possess mesoporosity as well as certain macroporosity and essentially maintain their pristine $CoCO_3$ morphologies unaltered. Because high crystal uniformity and high specific surface areas (140−149 $m^2/g$) have been achieved for this cobalt spinel, the gas sensors fabricated from the mesoporous $Co_3O_4$ powders have shown excellent sensing properties to ethanol and carbon monoxide, especially the low detection limits found for both gases.

**Acknowledgment.** The authors gratefully acknowledge the financial supports provided by the National University of Singapore, Economic Development Board, Singapore, and the King Abdullah University of Science and Technology, Saudi Arabia. C.C.L. would also like to thank the China Scholarship Council (CSC) for providing his exchange scholarship for Ph.D. study at the National University of Singapore.